Electron Energy Loss Spectroscopy of a Chiral Plasmonic Structure

2015 J. Phys.: Conf. Ser. 644 012005

(http://iopscience.iop.org/1742-6596/644/1/012005)

Electron Energy Loss Spectroscopy of a Chiral Plasmonic Structure

G W Paterson[1], A Karimullah[2], S D R Williamson[1], M Kadodwala[2] and D A MacLaren[1]

[1] SUPA, School of Physics and Astronomy, University of Glasgow, Glasgow G12 8QQ, UK.
[2] School of Chemistry, University of Glasgow, Glasgow G12 8QQ, UK.

E-mail: gary.paterson@glasgow.ac.uk

Abstract. A detailed analysis of the plasmonic excitations within a nanopatterned gold chiral biosensor element, measured by scanning transmission electron microscopy electron energy loss spectroscopy, is presented. We discuss aspects of data acquisition, processing, analysis and simulation. The localised surface plasmonic resonance modes in the structure are extracted using non-negative matrix factorisation and we use simulations to correlate notable deviations from the idealised spectrum to nanometric fabrication imperfections. The methodology presented has wide applicability to a variety of metamaterials.

1. Introduction

Plasmonic metamaterials have a diversity of applications, spanning optoelectronics, sensors and biomedicine. Their functionality derives from a precise control of patterned media down to the nanoscale, which can be difficult to assess with optical techniques. Energy loss spectroscopy (EELS) performed in a scanning transmission electron microscope (STEM), on the other hand, has ample spatial resolution but one can struggle to assess the plasmonic energy range associated with optical excitations because of the energy spread of the source and the proximity of the plasmon signal to the zero loss peak (ZLP). Motivated by recent work showing that chiral metamaterials can be used as a sensor of biomolecules [1], here we study a chiral nanostructure with STEM-EELS. A discussion of the chiral fields produced by such structures can be found elsewhere [2]. We present direct, nanometric maps of the localised surface plasmon resonance (LSPR) modes. Comparisons of experimental results to simulations enable the correlation of fabrication imperfections to the plasmonic properties.

2. Methodology

The structure under study, an approximately 60 nm thick, 500 nm diameter gold 'nanoswirl' was formed on a silicon nitride (SiN) window using electron beam lithography and e-beam evaporation with a 2 nm Ti adhesion layer. Figures 1(a) and (b) show the typical structure of the Au plasmonic element, which is markedly different to the ideal structure shown in Fig. 1(e). The edge-profile of the fabricated structure is tapered due to the metal deposition method used and the central region is enlarged because of overexposure of the resist during lithographic patterning; both aspects are a consequence of the relatively small feature sizes in the structure. In the central region, the thickness is relatively uniform and close to the nominal value, but notable thickness

variations and a loss of edge definition occur along the arms, partly due to the Au grain structure. Deviations from the ideal square-edged profile of the geometric design break the symmetry of the nanostructure and alter its plasmonic response, so it is essential to assess their impact. To do this we performed EELS measurements in a probe corrected JEOL ARM200F scanning transmission electron microscope operated at 200 keV and equipped with a cold field emission electron gun and a GIF Gatan Quantum ER spectrometer. The EELS data were collected at a dispersion of 0.025 eV/channel and spatial resolution of 3 nm. The dwell time was 50 ms and the convergence and collection semi-angles were 29 and 36 mrad. The thickness of the structure was extracted using the t/λ method [3], in which t is the thickness and λ is the inelastic mean free path, and was then used to form a mesh for use in the MNPBEM Matlab toolbox with EELS classes [4]. All data were analysed and processed in Python using the Hyperspy package [5].

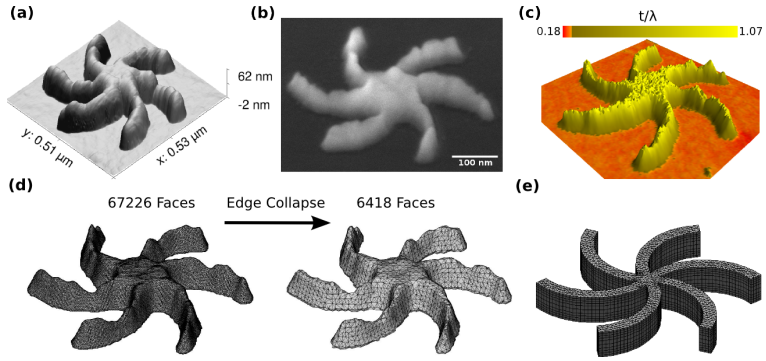

Figure 1. Typical nanoswirl plasmonic elements imaged by (a) AFM, (b) SEM (17.5 kV, 52° tilt), and, (c) EELS t/λ. In (d) and (e) are surface meshes of the t/λ data for the experimental structure and the surface mesh of the ideal 60 nm thick nanoswirl. Data were taken of different elements of the design.

3. Results & Discussion

An unexpected artefact in the data was a small lateral shift of the STEM diffraction disk as the beam scanned across the sample, because the projection system was not perfectly coupled to the microscope's diffraction plane. This can usually be corrected by post acquisition realignment of the EELS spectra, shifting spectra a few pixels along the dispersion direction. However, the weak plasmon signal lies close to the intense ZLP, so an artefact can arise if it overlaps with the ZLP afterglow of a previous spectrum. The shift in the beam position is approximately described by a plane, as shown in Figure 2(a). Thus, during a line-scan with small step size, continual drift of the beam results in the afterglow lying within the ZLP and the effect is only to broaden the peak slightly. However, at the beginning of a new line-scan, a larger offset in the beam position occurs. In the example data of Figure 2(a), the maximum shift of the ZLP is around 3 eV and results in a peak in subsequent spectra at similar energies and of similar intensities to the plasmon signal, as shown in Figure 2(b). To counteract this, spatial drift correction was employed at the end of every scan line, which allowed sufficient time for the afterglow to decay to insignificant levels. The effect of the artefact is seen as horizontal banded lines of decaying intensity in Figure 2(c), for which drift correction was used every fourth row. Only those rows acquired immediately after drift correction are free from afterglow artefacts. An alternative method for reducing the impact of the artefact would be to choose (in our case to reverse) the scan direction so that the afterglow falls on the energy gain side of the ZLP, which also has the advantage of not decreasing the rate at which data can be collected.

Next we discuss how the EELS data were processed to extract the plasmonic properties. The energy resolution of the EELS measurements is determined by the full width half maximum (FWHM) of the ZLP and is typically around 0.35 eV. To improve the energy resolution, Richardson-Lucy deconvolution [6] was used to narrow the FWHM of the ZLP to 0.11 eV. The deconvolved

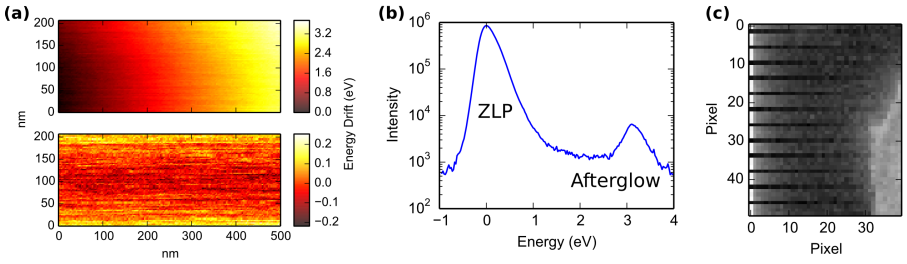

Figure 2. (a) Example sections of ZLP energy drift with scan position as measured (top) and after plane subtraction (bottom). (b) Spectra showing an afterglow artefact at the start of a new line-scan. (c) Maximum intensity on a log scale in a window covering the energy range of the artefact at different scan positions. The horizontal bands in (c) are due to drift correction allowing time for the afterglow to deminish to insignificant levels.

data were then processed using non-negative matrix factorisation [7] (NMF), a multivariate decomposition technique which has been successfully used to extract plasmonic modes [8]. An advantage that NMF holds over other decomposition protocols is that it restricts the components to be positive and so is constrained to produce spectral components that are often more representative of the real excitations. Typical results of performing factorisation of the nanoswirl dataset with 4 components is shown in Figure 3, with the decomposition factors (DFs) and loadings (DLs) in panels (a) and (b). The decomposition components are readily identified from the spatial distributions [Fig. 3(b)] and compare reasonably well with excitations observed in the unprocessed data. The first component, DL0, is a background signal localised within the gold and corresponds to a broadening of the ZLP. The fourth component is delocalised across the entire structure and corresponds to the leading edge of a bulk plasmon. Of greater significance are DL1 and DL2, modes with losses concentrated at the tips and base of the swirl, respectively. These can be seen as diffuse intensity outside of the main structure, at locations indicated by red arrows. The double peak in component 2 indicates that two modes are being extracted as one component. An example of the influence of the structural imperfections is the greater loss at the tips of the vertical arms in DL1, which would not occur in a symmetric structure.

To explore the influence of the structural imperfections on the plasmonic modes, we performed simulations of different structures using the MNPBEM toolbox [4]. The mesh of the ideal structure was generated directly in the toolbox and is shown in Figure 1(e). Forming a surface mesh of the exact structure requires additional tools and we did this by first determining the structure from the sample thickness, measured using the t/λ method [3]. Figure 1(c) shows the t/λ values calculated after extrapolating the spectra to higher energies using a power law. With the substrate thickness removed by subtracting a plane fitted to the masked surface to select

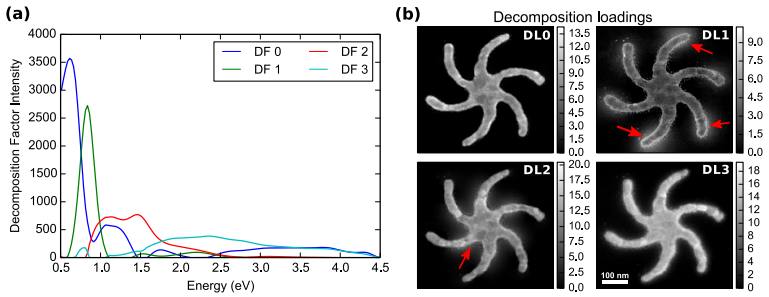

Figure 3. NMF of EELS spectra from a Au nanoswirl metamaterial element, showing (a) the factors and (b) the loadings corresponding to the characteristic spectra and spatial distributions, respectively.

only the bare SiN region, the Au t/λ values were then converted to absolute thicknesses using the Iakoubovskii form for $\lambda(\rho)$ [9] with a density, ρ, of 19.3 g/cm^3, giving a λ of 90.9 nm. To create the surface mesh, the metal thickness map was converted into a discretised binary volume after gently smoothing the data by 2-D gaussian convolution, and then to a 2-D surface mesh using a marching cubes algorithm. This mesh was then simplified by edge collapse, with the resulting meshes shown in Fig. 1(d).

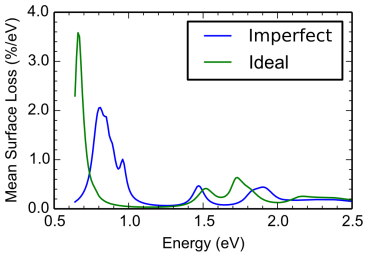

Figure 4. Simulated surface loss spectra from the imperfect and ideal structures, using the MNPBEM toolbox with tabulated values for Au permittivity. The substrate and adhesion layer were omitted for computational ease.

Finally, in Figure 4 the results of the simulations are compared. As a direct result of symmetry reduction due to structural imperfections, there are significant changes in the peak intensities and energies. The first peak is particularly strongly affected, with the single LSPR mode in the ideal structure split into a number of modes in the imperfect structure. The simulations of the imperfect structure compare favourably with the experimental data of Fig. 3. The different mode energies in the simulation may be related to the omission of the substrate and adhesion layer in the simulated structures.

4. Conclusions

The impact of structural imperfections on the plasmonic excitations of nanostructured materials can be assessed directly using EELS. Having knowledge of the precise, imperfect structure under study allows the effect of structural imperfections to be determined through simulation. Our results demonstrate that EELS is invaluable for simultaneously characterising the structural and the plasmonic properties, both in space and energy, of such nanostructures. With the advent of monochromated TEM instruments, the prospect for extending this work to a multitude of plasmonic metamaterial elements is an exciting one.

Acknowledgements

This work was funded by the Engineering and Physical Sciences Research Council (EPSRC) of the UK (EP/L001969/1). Original data files are available at: http://dx.doi.org/10.5525/gla.researchdata.195.

References

[1] Hendry E, Carpy T, Johnston J, Popland M, Mikhaylovskiy R V, Lapthorn A J, Kelly S M, Barron L D, Gadegaard N and Kadodwala M 2010 *Nat. Nano* **5** 783
[2] Schäferling M, Dregely D, Hentschel M and Giessen H, 2012 *Phys. Rev. X* **2** 031010
[3] Egerton R F 2011 *Springer, New York*
[4] Hohenester U 2014 *Computer Physics Communications* **185** 1177
[5] Hyperspy: A toolbox for hyperspectra data analysis *http://hyperspy.org*
[6] A. Gloter A, Douiri A, Tencé M and Colliex C 2003 *Ultramicroscopy* **96** 385
[7] Lee D D and Seung H S 1999 *Nature* **401** 788
[8] Nicoletti D, Peña F. de la, Leary R K, Holland D J, Ducati C and Midgley P A 2013 *Nature* **502** 80
[9] Iakoubovskii K, Mitsuishi K, Nakayama Y, Furuya K 2008 *Microsc. Res. Tech.* **71** 626